

Single-Molecule Junctions

Distinct Charge Transport and its Regulation in Single-Molecule and Monolayer Junctions

Lan Yang⁺, Cong Zhao⁺, Ju Wang⁺, Feifan Yue, Zhehao He, Mingliang Li,^{*} Guangwu Li,^{*} Jinying Wang,^{*} Chuancheng Jia,^{*} and Xuefeng Guo^{*}

Abstract: As electronic devices miniaturize to the nanometer scale, molecular junctions, including single and monolayer molecules, are gaining attention for applications in logic, storage, and sensing. However, comparative studies of charge transport in these two junction types are limited. Here, a highly conjugated pyrene derivative has been engineered to construct both single-molecule and monolayer junctions. The charge transport within these junctions has been examined systematically through theoretical simulations and electrical measurements. These studies demonstrate a distinct transition in a single molecule from temperature-independent coherent tunneling to temperature-dependent incoherent transport, indicating vibration-mediated transport, while vibration-suppressed coherent transport is observed in a densely packed monolayer. Additionally, anisotropic gating experiments reveal that parallel fields relative to the molecular connection modulate energy levels more efficiently in comparison with perpendicular fields. These findings enrich our understanding of molecular electronic transport and pave the way for diverse developments in the field of molecular electronic devices.

Introduction

Advancements in molecular electronics, utilizing molecules as basic building units, have emerged as a promising solution to overcome the physical limitations faced by traditional silicon-based technologies.^[1–4] Core technologies within this field can be divided into two categories: single-molecule junctions (SMJs)^[3,5–7] and monolayer junctions (MJJs),^[8–12] collectively referred to as single-molecule devices. These devices, with

their sub-5 nm molecular architectures, provide an ideal platform to explore the transition from quantum to classical transport and develop logic elements at the molecular scale. Understanding their charge transport properties, particularly the temperature-dependent behavior and the influence of external fields, remains a significant challenge that requires further investigation. SMJs and MJJs, despite sharing similar transport mechanisms like coherent tunneling, incoherent tunneling, and hopping, differ significantly due to variations in their local environments,^[13] such as molecule-electrode interactions, molecular arrangements, and intermolecular interactions. For SMJs, charge transport is governed by the single-molecule property and their interaction with the electrodes, without considering intermolecular interactions, thus allowing for the detection of individual events.^[14–16] In contrast, MJJs consist of a molecular monolayer, where intermolecular interactions and collective electrostatic effects play a crucial role, leading to uniform charge transport influenced by molecular arrangement and polarization.^[16] For example, collective electrostatic effects lead to notable differences in conductance between SMJs and MJJs.^[17] In addition, studies have shown that intermolecular quantum interference effects within the monolayer can influence the transport mechanisms.^[18] While much research has been conducted on the charge transport properties of SMJs^[19,20] and MJJs^[21] individually, comparative studies encompassing both are scarce.


The charge transport mechanisms in these devices can be primarily characterized through temperature- and voltage-dependent electrical measurements. Coherent transport processes typically exhibit temperature independence, while other processes like heat-assisted tunneling, hopping, and thermionic emission show distinct temperature dependence.^[14,15] In SMJs, many studies have demonstrated

[*] L. Yang⁺, C. Zhao⁺, J. Wang⁺, F. Yue, Z. He, Prof. G. Li, Prof. J. Wang, Prof. C. Jia, Prof. X. Guo
 Center of Single-Molecule Sciences, Institute of Modern Optics, Frontiers Science Center for New Organic Matter, Tianjin Key Laboratory of Microscale Optical Information Science and Technology, College of Electronic Information and Optical Engineering, Nankai University, 38 Tongyan Road, Jinnan District, Tianjin 300350, P.R. China
 E-mail: ligw@nankai.edu.cn
 wangjynk@nankai.edu.cn
 jiacc@nankai.edu.cn
 guoxf@pku.edu.cn

Dr. M. Li
 Department of Chemistry, The University of Hong Kong, Chong Yuet Ming Chemistry Building, Pokfulam Road, Hong Kong 999077, P.R. China
 E-mail: liml@hku.hk

Prof. X. Guo
 Beijing National Laboratory for Molecular Sciences, National Biomedical Imaging Center, College of Chemistry and Molecular Engineering, Peking University, 292 Chengfu Road, Haidian District, Beijing 100871, P.R. China

[⁺] These authors contributed equally to this work.

 Additional supporting information can be found online in the Supporting Information section

that molecular vibrations coupled to electronic transport often lead to the pronounced temperature-dependent behavior.^[20,22] In contrast, MJs exhibit more complex temperature responses (Tables S1 and S2)^[11,23–26] For instance, systems with densely packed structures generally exhibit a negligible temperature dependence due to limited intermolecular spacing that suppresses thermally activated transport.^[11,23] In contrast, the incorporation of bulky terminal groups, such as π -conjugated or metal-coordination units,^[24,25] can disrupt molecular packing regularity, increase intermolecular spacing, and thereby introduce a temperature-dependent transport behavior. These variations underscore the importance of comparative studies on temperature-dependent mechanisms in SMJs and MJs. In addition, electric fields—such as the source-drain bias and gate voltage—can modulate transport channels and charge distribution, providing insights into molecular electronic states,^[27] vibrational modes,^[28] and spin properties.^[29] A powerful method to probe these effects is Coulomb-diamond mapping, which involves measuring current or differential conductance at low temperatures while sweeping both the bias and gate voltages. For example, in SMJs, Coulomb-diamond analysis reveals energy-level alignment and thermal activation processes.^[30] However, how field alignment enables precise molecular manipulation remains unclear. Current studies have primarily focused on electric fields applied along forward and reverse directions,^[31] while the effects of perpendicular or cross-directional fields constitute a significant research gap. This mechanistic gap necessitates further research, particularly into gate-field-orientation modulation of the molecular energy levels.

To address these challenges, we have developed a dual-platform strategy that utilizes pyrene-core devices, specifically graphene-based SMJs and vertically stacked molecular junctions MJs. Our design systematically investigates the effects of molecular vibration on charge transport through comparative studies of a single molecule and a densely packed monolayer. Furthermore, this approach allows for investigating the anisotropic gate-control mechanisms by applying electric fields along two orthogonal orientations relative to the molecular junction. Our findings are crucial for advancing our understanding of transport mechanisms in molecular devices. Moreover, they contribute to the advancement of various technological applications and practical implementations in molecular electronics.

Results and Discussion

Fabrication of SMJs and MJs

In this study, the molecule 4,4'-(pyrene-1,6-diylbis(ethyne-2,1-diyl)) dianiline (PDE) (Figures 1a and S1–S3, detailed synthesis procedures are described in the Supporting Information), with amino groups at both ends, is covalently connected to graphene electrodes to form a SMJ (Figure 1b). The amino groups can also serve as anchoring groups, allowing these molecules to form self-assembled monolayers (SAMs) on the gold surface, thus constructing MJs (Figure 1c). Pyrene is selected as the core due to its exceptional

performance as a well-known chromophore and an excellent electron donor. Its large π -conjugated structure ensures strong light-harvesting capabilities and efficient electron-transfer properties.^[32] The benzene rings and alkyne groups function as spacer groups, which promote a configuration that facilitates moderate coupling between pyrene and electrodes while concurrently maintaining the overall rigidity of the junctions. In addition, triisopropyl((4-((7-(phenylethynyl)pyren-2-yl)ethynyl)phenyl)ethynyl)silane (PPE) molecule with different anchoring group is used as a control (Figures S4–S7, detailed synthesis procedures are described in the Supporting Information). The fabrication of SMJs and MJs is described in the Materials and Methods Section, with the characterization of the SAM provided in Figure S8. Diethyl (2-methoxyethyl) ammonium bis (trifluoromethylsulfonyl) imide (DEME-TFSI) ionic liquid is utilized in both SMJs and MJs to provide gate modulation. This ionic liquid, characterized by a large electrochemical window,^[33] forms a double-layer structure on both the surface of graphene-based SMJs and the top graphene electrode of vertical tunneling MJs. This double layer can generate an electric field of up to 10 MV cm^{-1} ,^[34] effectively modulating the alignment of the molecular orbitals.

Temperature-Dependent Measurements

To explore the charge transport mechanisms in PDE SMJs and MJs, temperature-dependent current measurements were conducted. The I_D – V_D curves were scanned under high-vacuum conditions within a temperature range of 100–300 K. As the temperature decreases from 300 to 100 K, the current in SMJs decreases significantly, showing an approximately six-fold decrease at a bias voltage of 1 V (Figure 2a). In contrast, the current in MJs remains relatively stable over the same temperature range (Figure 2d).

To elucidate the differences in charge transport mechanisms between SMJs and MJs, an Arrhenius analysis of the I_D – V_D data was conducted. The Arrhenius plots for SMJs, derived from the I_D – V_D curves, reveal two distinct regions: (I) a region with significant temperature dependence, and (II) a region without temperature dependence (Figure 2b). The transition temperature between these two regions is 220 K. Conversely, SAMs exhibit consistently weak temperature dependence across all examined temperatures (Figure 2e). To verify the reliability of this phenomenon, the temperature dependence on other devices is examined as shown in Figure S9. According to the thermal activation formula,^[35] the thermal activation energies can be calculated. The thermal activation energies for the high-temperature and low-temperature regions in the SMJ under a bias voltage of -0.1 V are determined to be 147.72 and 6.05 meV (nearly zero), respectively (Figure 2c). These results indicate that the activation energy in the high-temperature region is substantially higher than that in the low-temperature region. For MJs, the activation energy remains below 1 meV over a bias voltage range of -0.1 to -1 V (Figure 2f). Therefore, it can be demonstrated that in SMJs, the transport mechanism transitions from heat-assisted incoherent

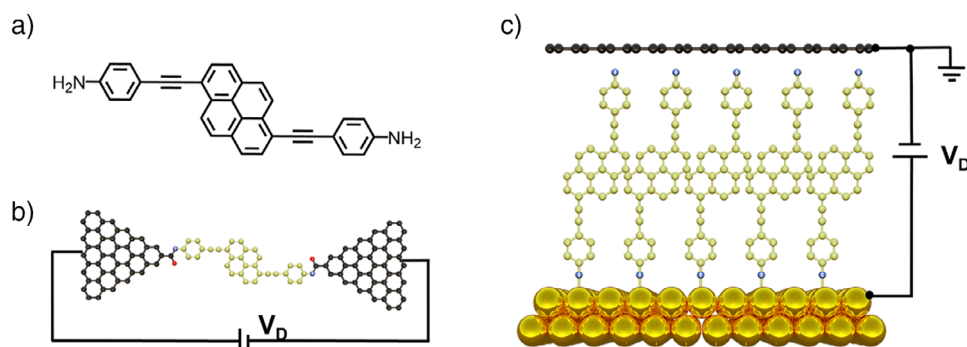


Figure 1. Schematic diagram of SMJ and MJ devices. a) The chemical structure of the PDE molecule. b) Diagram of the graphene-based SMJ with PDE. c) Schematic diagram of the MJ based on PDE SAMs.

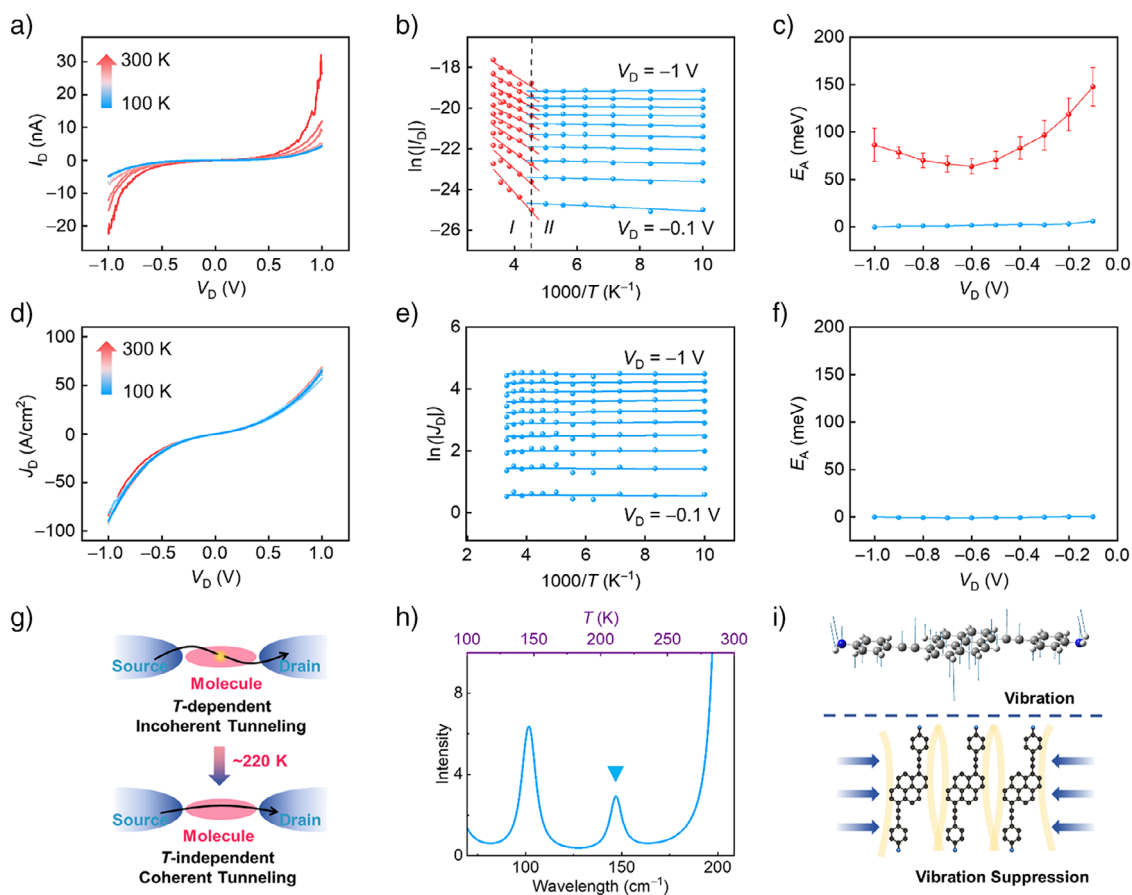


Figure 2. Temperature-dependent charge transport characteristics. a) and d) Temperature-dependent I - V curves for a) SMJs and d) MJs. b) and e) Arrhenius plots of $\ln(|I_D|)$ or $\ln(|J_D|)$ versus $1/T$ for b) SMJs and e) MJs under negative biases at a step of 0.1 V. c) and f) Bias-dependent activation energies for c) SMJs and f) MJs, where regions I and II represent the high-temperature-dependent and low-temperature-independent regions, respectively. g) Schematic diagram of charge transport transition mechanism. h) The theoretical vibrational spectrum of pyrene. i) Schematic diagram for the vibrational modes corresponding to the transition temperature of a single pyrene molecule and its vibrational suppression in a SAM.

tunnelling at high temperatures to temperature-independent coherent transport at low temperatures.^[36] In contrast, MJs exhibit only temperature-independent coherent tunnelling across the examined temperature range.

The transition temperature between coherent and incoherent transport is crucial for understanding the structure-property relationship in intermolecular charge transport

mechanisms.^[14] It is significantly influenced by specific molecular vibrational modes in molecular junctions.^[20,22,37–39] To further elucidate the disparate charge transport mechanisms exhibited by SMJs and MJs, the vibrational spectra of PDE molecules were calculated and analyzed (Figure 2h). The vibrational modes corresponding to each peak are identified. According to the conversion relation between transition

temperature and vibrational energy ($k_B T_{\text{trans}} = h\nu$), the benzene-pyrene coupled rotation at 147.3 cm^{-1} aligns with the thermal activation energy at the experimental transition temperature of 220 K. Notably, within the vibrational spectrum corresponding to the temperature range under investigation, two peaks are observed at 101.7 and 147.3 cm^{-1} , both of which correspond to the coupled vibrations between the benzene and pyrene. To further investigate the effects of these vibrations, calculations of the transmission spectrum for the molecules were performed using the Quantum Atomistix Toolkit package (ATK, modeling as shown in Figure S10). This was done while maintaining consistent orbital energy levels calculated by both Gaussian and ATK (Figure S11). The peak at 101.7 cm^{-1} consists of two closely spaced modes at 100.1 and 102.9 cm^{-1} . The 100.1 cm^{-1} mode corresponds to out-of-plane vibrations of the pyrene core (Figure S12a). Transmission spectra calculated at the extremities of this mode show no change in the HOMO and LUMO energy levels (Figure S12d), indicating that it has a negligible effect on the charge transport properties. The 102.9 cm^{-1} mode involves rotational motions of the terminal phenyl ring (Figure S12b), which does not disrupt the π -conjugation. Calculations also show no shift in the HOMO and LUMO levels (Figure S12e), confirming its negligible impact on charge transport. In contrast, the 147.3 cm^{-1} mode involves out-of-plane motions of both pyrene and phenyl units (Figure S12c). This vibration perturbs the conjugation pathway, and calculations reveal shifts in the HOMO and LUMO levels (Figure S12f), indicating its significant role in modulating charge transport in SMJs. In MJJs, the dense molecular packing suppresses these vibrations, leading to temperature-independent coherent tunneling (Figure 2i). To further explore this effect, the vibrational spectra for the systems consisting of two and three PDE molecules were calculated. A blueshift of the characteristic vibrational peaks is observed with increasing the packing density, and the corresponding peak intensities deviate from a linear increase (Figure S13). These results suggest that close molecular stacking can suppress the out-of-plane motions of both pyrene and phenyl units in the PDE molecules. While previous studies have reported similar views,^[19] this work uniquely combines theoretical calculations with experiments to clarify the role of molecular vibrations in charge transport. It offers deeper mechanistic insights and quantitative analysis of vibrational effects. These findings provide a clearer understanding of molecular electronic transport under varying environments and external fields, advancing the field toward precise control and functional device design.

Gate-Dependent Measurements

To investigate the field-effect transistor properties of molecular junctions, DEME-TFSI ionic liquids were employed for gating (Figures 3a,b, S14, and S15).^[40] It is noteworthy that the gate fields, formed by the double layer in the ionic liquid, differ between the two technologies. In the SMJ, the gate-field direction is perpendicular to the axis of molecular connection, whereas it is parallel in the MJ.

The gate-dependent performance of both SMJs and MJJs was measured under ultra-high vacuum at 200 K. Figure 3c,d display the typical gate-dependent characteristics of SMJs and MJJs, respectively. The reproducible field-effect characteristics for some other devices are shown in Figure S16. As the gate voltage varies from -3 to 3 V , both the current $|I_D|$ in the SMJ and the current density $|J_D|$ in the MJ initially decrease and then increase, indicating that both techniques enable efficient gate modulation.

The two-dimensional conductance mapping, represented as dI/dV versus V_G and V_D , reveals that both SMJs and MJJs exhibit single-electron transport characteristics (Figure 3e,f).^[41,42] Low-conductance regions are depicted in blue and green, while high-conductance regions are shown in red. A complete Coulomb diamond is observed in the MJ within the tested range of bias and gate voltages, while no complete Coulomb diamond appears for the SMJ. Furthermore, gate-modulation measurements conducted at both 220 and 300 K reveal consistent trends (Figures S17 and S18), with MJJs exhibiting a stronger gate tunability in comparison with SMJs. Upon fitting the slopes of the Coulomb diamonds in SMJs and MJJs, the molecular capacitances (C_G) are 0.24 and 0.25 e V^{-1} , the source-electrode capacitances (C_S) are 0.87 and 0.60 e V^{-1} , and the drain-electrode capacitances (C_D) are 0.74 and 0.35 e V^{-1} , respectively. The charging energies $E_C = e^2/[2(C_G + C_S + C_D)]$ for the two junctions are calculated to be 0.27 and 0.42 eV , respectively. The similarity in molecular capacitances confirms the signal's origin in the molecule. The MJ exhibits more distinct C_S and C_D and a higher E_C than the SMJ due to the different electrode materials and weaker π -electrode interactions.^[41] By analyzing the intersections of the diamond edges, the addition energy (E_{add}) for the MJ is found to be 1.07 eV . Using $E_{\text{add}} = E_C + \Delta E$, E_{add} for the SMJ is estimated to be 3.10 eV , with ΔE approximated by the molecular HOMO-LUMO gap of 2.83 eV (Figure 4a),^[41] which is consistent with the experimental results. For the MJ, ΔE is calculated to be 0.65 eV , significantly smaller than the HOMO-LUMO gap due to energy level broadening in SAMs (Figure 4b). Furthermore, the total gate coupling efficiency $b = C_G/(C_G + C_S + C_D)$ of the SMJ ($b = 0.13$) is lower than that of the MJ ($b = 0.21$), indicating less effective gate modulation in the SMJ. In addition, both SMJs and MJJs exhibit minimal differences in the gate coupling efficiency between 300 and 220 K, indicating the robust gating performance of ionic liquids at cryogenic temperatures, consistent with the previous report.^[43]

To further elucidate the mechanism of different gate-regulation capacities, the effect of external electric field directions was simulated and analyzed. When the external electric field is oriented perpendicularly to the molecular junction (E_y), the HOMO-LUMO gap remains constant, regardless of the increase in electric field strength (Figure 4c). However, when the electric field is applied parallel (E_x) to the molecular junction, it significantly decreases (Figure 4d). Therefore, it can be inferred that the differing gate-regulation capacities mainly stem from the varying impacts of directions of the electric field on molecular orbitals. In addition, considering that molecular orientations may exhibit a finite

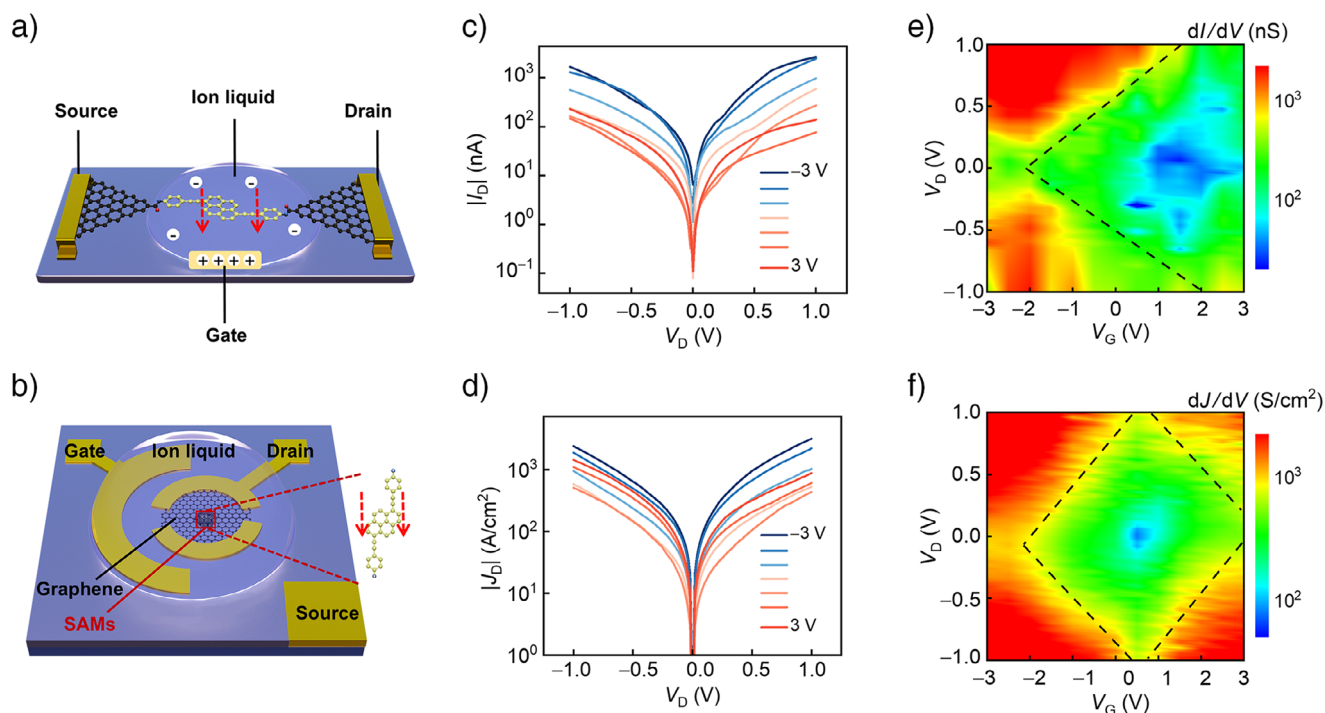


Figure 3. Field-effect characteristics of SMJ and MJ devices. a) and b) Schematic illustration of the a) SMJ and b) MJ structure with ionic liquid gating. c) $|I_D|$ versus V_D characteristics of SMJs with V_G varying from -3 to 3 V at a step of 1 V. d) $|J_D|$ versus V_D characteristics of MJs with V_G varying from -3 to 3 V at a step of 1 V. e) and f) Two-dimensional visualizations of e) dI/dV plotted versus V_G and V_D for SMJs and f) dJ/dV plotted versus V_G and V_D for MJs. The black dashed lines represent auxiliary markers on the diamond-shaped edges of conductivity.

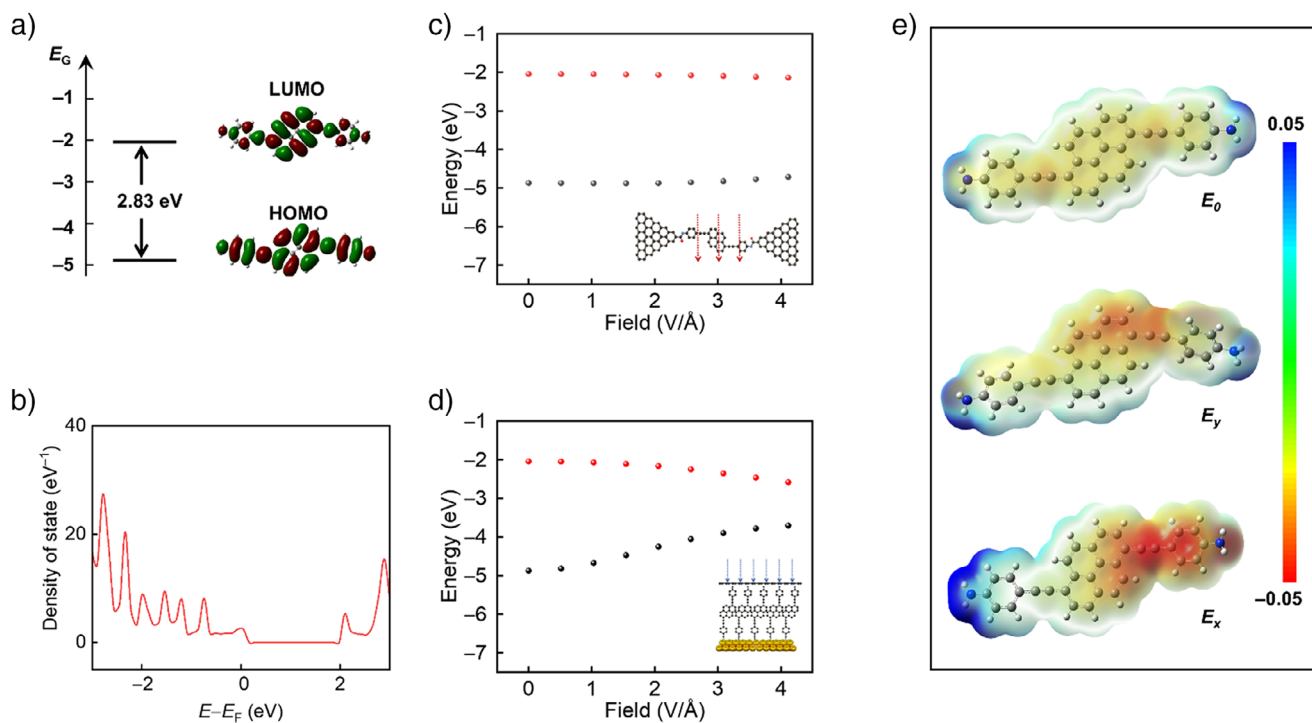


Figure 4. Theoretical calculation of the electrostatic potential and energy levels of the PDE molecule. a) The energy levels of the frontier orbitals of a single PDE molecule. b) DOS calculation of PDE SAMs. c) Gate regulation of frontier orbitals in SMJs. d) Gate regulation of frontier orbitals in MJs. e) Calculated mapping of molecular electrostatic potential under E_y and E_x electric fields with the same iso-value.

tilt angle relative to the field direction, theoretical calculations were performed to investigate the electric-field modulation for molecules oriented at specified angles. The results indicate that even in non-parallel configurations, a significant difference in modulation between the E_x and E_y directions persists (Figure S19). This supports the validity and robustness of our directional gate-control analysis under idealized assumptions. Meanwhile, electrostatic potential mapping of the molecules under E_y and E_x electric fields has also been calculated (Figure 4e). It can be seen that the E_x electric field has a greater impact on the molecular electrostatic potential than the E_y electric field. This difference contributes to varying capacities for gate regulation, and these findings are consistent with experimental observations. To validate the generality of this phenomenon, calculations are extended to compare the directional electric field responses of alkyl chains and phenylacetylene systems with varying lengths. The results consistently show that modulation along the E_x direction produces a stronger effect, thus highlighting the universal nature of this behavior across different molecular backbones and chain lengths (Figure S20).

Conclusion

In this work, we fabricated both SMJs and MJJs based on PDE molecules and systematically investigated their charge transport properties, employing temperature and gate voltage as modulation parameters. In SMJs, a clear transition from temperature-independent coherent tunneling to temperature-dependent incoherent transport occurs with increasing temperature. Conversely, MJJs do not exhibit a temperature-dependent behavior. This is due to the suppression of vibrations from individual molecules in assemblies characterized by high molecular density. Furthermore, by constructing a three-terminal device using ionic liquids, the impact of gate direction on the energy-level regulation of the PDE molecule is examined. It is found that gate regulation is more effective when the electric field is parallel to the molecular connection in comparison with the case when it is vertical, proving the critical role of benzene-pyrene coupled vibrations in transport mechanism switching. These findings elucidate the critical role of the molecular environment in modulating vibration-assisted tunneling, as well as the pronounced influence of electric field orientation on the regulation of molecular energy levels. Such insights are essential for a deeper understanding of charge transport mechanisms in molecular systems and offer guiding principles for the design of efficient, controllable, and scalable molecular-scale electronic components, thereby advancing the development of next-generation miniaturized electronic devices.

Supporting Information

Experimental methods; characterization; additional experimental data and calculation data. The authors have cited additional references within the Supporting Information.

Acknowledgements

The authors acknowledge financial support from the National Key R&D Program of China (2024YFA1208100, 2021YFA1200102, 2021YFA1200101, 2023YFF1205803, and 2022YFE0128700), the National Natural Science Foundation of China (22173050), and Beijing National Laboratory for Molecular Sciences (BNLMS-CXXM-202407).

Conflict of Interests

The authors declare no conflict of interest.

Data Availability Statement

The data that support the findings of this study are available from the corresponding author upon reasonable request.

Keywords: Charge transport • Gate-voltage regulation • Monolayer junctions • Single-molecule junctions • Vibration-assisted tunneling

- [1] M. Ratner, *Nat. Nanotechnol.* **2013**, *8*, 378–381.
- [2] P. T. Mathew, F. Z. Fang, *Engineering* **2018**, *4*, 760–771.
- [3] D. Xiang, X. L. Wang, C. C. Jia, T. Lee, X. F. Guo, *Chem. Rev.* **2016**, *116*, 4318–4440.
- [4] I. Stone, R. L. Starr, Y. P. Zang, C. Nuckolls, M. L. Steigerwald, T. H. Lambert, X. Roy, L. Venkataraman, *Nat. Rev. Chem.* **2021**, *5*, 695–710.
- [5] Y. Li, C. Yang, X. F. Guo, *Acc. Chem. Res.* **2020**, *53*, 159–169.
- [6] S. V. Aradhya, L. Venkataraman, *Nat. Nanotechnol.* **2013**, *8*, 399–410.
- [7] L. Yang, Z. Z. Zhang, C. Zhao, N. Y. Huo, E. Y. Zhang, S. H. He, C. C. Jia, X. F. Guo, *Chin. J. Chem.* **2023**, *41*, 2889–2907.
- [8] R. M. Metzger, *Chem. Rev.* **2015**, *115*, 5056–5115.
- [9] A. Salomon, D. Cahen, S. Lindsay, J. Tomfohr, V. B. Engelkes, C. D. Frisbie, *Adv. Mater.* **2003**, *15*, 1881–1890.
- [10] Y. M. Han, C. Nickle, Z. Y. Zhang, H. P. Astier, T. J. Duffin, D. C. Qi, Z. Wang, E. D. Barco, D. Thompson, C. A. Nijhuis, *Nat. Mater.* **2020**, *19*, 843–848.
- [11] C. C. Jia, M. Famili, M. Carloti, Y. Liu, P. Q. Wang, L. M. Grace, Z. Y. Feng, Y. L. Wang, Z. P. Zhao, M. L. Ding, *Sci. Adv.* **2018**, *4*, eaat8237.
- [12] C. C. Jia, L. M. Grace, P. Q. Wang, A. Almeshal, Z. H. Huang, Y. L. Wang, P. Chen, L. Y. Wang, J. Y. Zhou, Z. Y. Feng, *Chem.* **2020**, *6*, 1172–1182.
- [13] A. Landau, L. Kronik, A. Nitzan, *J. Comput. Theor. Nanosci.* **2008**, *5*, 535–544.
- [14] Y. Selzer, L. Cai, M. A. Cabassi, Y. Yao, J. M. Tour, T. S. Mayer, D. L. Allara, *Nano Lett.* **2004**, *126*, 4052–4053.
- [15] Z. X. Chen, S. L. Woltering, B. Limburg, M. Y. Tsang, J. Baugh, G. A. D. Briggs, J. A. Mol, H. L. Anderson, J. O. Thomas, *Angew. Chem. Int. Ed.* **2024**, *63*, e202401323.
- [16] V. Ayelet, D. Aswal, D. Cahen, *Chem. Rev.* **2017**, *117*, 4248–4286.
- [17] V. Obersteiner, D. A. Egger, E. Zojer, *J. Phys. Chem. C* **2015**, *119*, 21198–21208.
- [18] P. A. Li, Y. Selzer, *Nat. Commun.* **2022**, *13*, 4742.
- [19] N. Xin, X. X. Li, C. C. Jia, Y. Gong, M. L. Li, S. P. Wang, G. Y. Zhang, J. L. Yang, X. F. Guo, *Angew. Chem. Int. Ed.* **2018**, *57*, 14026–14031.

- [20] X. Zhu, B. Y. Wang, W. Xiong, S. Y. Zhou, K. Qu, J. T. Lü, H. L. Chen, C. C. Jia, X. F. Guo, *Angew. Chem. Int. Ed.* **2022**, *61*, e202210939.
- [21] S. K. Karuppannan, H. T. Hu, C. Troadec, A. Vilan, C. A. Nijhuis, *Adv. Funct. Mater.* **2019**, *29*, 1904452.
- [22] M. Zhang, B. Wang, H. Jia, X. Xie, J. Hao, L. Zhou, P. Du, J. Wang, C. Jia, X. Guo, *Adv. Sci.* **2025**, *12*, 2408310.
- [23] X. P. Chen, B. Kretz, F. Adoah, C. Nickle, X. Chi, X. J. Yu, E. D. Barco, D. Thompson, D. A. Egger, C. A. Nijhuis, *Nat. Commun.* **2021**, *12*, 3432.
- [24] Y. M. Han, C. Nickle, M. S. Maglione, S. K. Karuppannan, J. Casado-Montenegro, D. C. Qi, X. P. Chen, A. Tadich, B. Cowie, M. Mas-Torrent, *Adv. Sci.* **2021**, *8*, 2100055.
- [25] L. Yuan, L. Wang, A. R. Garrigues, L. Jiang, H. V. Annadata, M. A. Antonana, E. Barco, C. A. Nijhuis, *Nat. Nanotechnol.* **2018**, *13*, 322–329.
- [26] X. P. Chen, T. S. Zhang, X. J. Yu, I. Volkova, C. A. Nijhuis, *ACS Appl. Mater. Interfaces* **2020**, *12*, 45111–45121.
- [27] H. K. Park, J. Park, A. K. Lim, E. H. Anderson, A. P. Alivisatos, P. L. McEuen, *Nature* **2000**, *407*, 57–60.
- [28] E. A. Osorio, K. O'Neill, N. Stühr-Hansen, O. F. Nielsen, T. Bjørnholm, H. S. J. van der Zant, *Adv. Mater.* **2007**, *19*, 281–285.
- [29] A. S. Zyazin, J. W. V. D. Berg, E. A. Osorio, H. S. J. van der Zant, N. P. Konstantinidis, M. Leijnse, M. R. Wegewijs, F. May, W. Hofstetter, C. Danieli, *Nano Lett.* **2010**, *10*, 3307–3311.
- [30] P. Gehring, J. K. Sowa, C. W. Hsu, J. d. Bruijckere, M. v. d. Star, J. J. L. Roy, L. Bogani, E. M. Gauger, H. S. J. van der Zant, *Nat. Nanotechnol.* **2021**, *16*, 426–430.
- [31] A. C. Aragonès, N. L. Haworth, N. Darwish, S. Ciampi, E. J. Mannix, G. G. Wallace, I. Diez-Perez, M. L. Coote, *Nature* **2016**, *531*, 88–91.
- [32] J. M. Sun, H. S. Jena, C. Krishnaraj, K. S. Rawat, S. Abednatanzi, J. Chakraborty, A. Laemont, W. L. Liu, H. Chen, Y. Y. Liu, *Angew. Chem. Int. Ed.* **2023**, *62*, e202216719.
- [33] T. Sato, G. Masuda, K. Takagi, *Electrochim. Acta* **2004**, *49*, 3603–3611.
- [34] A. J. Bard, L. R. Faulkner, H. S. White, *Electrochemical Methods: Fundamentals and Applications*, John Wiley & Sons, Hoboken, **2022**.
- [35] D. Segal, A. Nitzan, M. Ratner, W. B. Davis, *J. Phys. Chem. B* **2000**, *104*, 2790–2793.
- [36] T. Hines, I. Diez-Perez, J. Hihath, H. M. Liu, Z. S. Wang, J. W. Zhao, G. Zhou, K. Müllen, N. J. Tao, *J. Am. Chem. Soc.* **2010**, *132*, 11658–11664.
- [37] N. Xin, C. C. Jia, J. Y. Wang, S. P. Wang, M. L. Li, Y. Gong, G. Y. Zhang, D. B. Zhu, X. F. Guo, *J. Phys. Chem. Lett.* **2017**, *8*, 2849–2854.
- [38] S. Q. Du, K. J. Yoshida, Y. Zhang, I. Hamada, K. Hirakawa, *Nat. Photonics* **2018**, *12*, 608–612.
- [39] W. K. Quan, Z. H. Wang, Y. Q. Shi, K. K. Liang, L. Y. Bi, H. Zhou, Z. Y. Yin, W. L. Li, S. W. Li, *J. Am. Chem. Soc.* **2025**, *147*, 4504–4510.
- [40] L. Zhou, M. Zhang, Y. N. Huo, L. P. Bai, S. H. He, J. Y. Wang, C. C. Jia, X. F. Guo, *Green Energy Environ.* **2024**, *9*, 1784–1801.
- [41] J. A. Mol, C. S. Lau, W. J. Lewis, H. H. Sadeghi, C. Roche, A. Cnossen, J. H. Warner, C. J. Lambert, H. L. Anderson, G. A. D. Briggs, *Nanoscale* **2015**, *7*, 13181–13185.
- [42] P. Gehring, A. Harzheim, J. Spiece, Y. W. Sheng, G. Rogers, C. Evangeli, A. Mishra, B. J. Robinson, K. Porfyrakis, J. H. Warner, *Nano Lett.* **2017**, *17*, 7055–7061.
- [43] J. R. Tian, C. J. Cui, Q. Xie, W. Z. Qian, C. Xue, Y. H. Miao, Y. Jin, G. Zhang, B. H. Guo, *J. Mater. Chem. A* **2018**, *6*, 3593–3601.

Manuscript received: April 19, 2025

Revised manuscript received: July 21, 2025

Accepted manuscript online: July 21, 2025

Version of record online: ■■■■■